Perfect crystal neutron loop cavity

Owen Lailey [1,2,*] Dusan Sarenac [3] David G. Cory [1,4] Michael G. Huber,[5] and Dmitry A. Pushin [1,2,†]

[1]*Institute for Quantum Computing, University of Waterloo, Waterloo, Ontario N2L3G1, Canada*

[2]*Department of Physics and Astronomy, University of Waterloo, Waterloo, Ontario N2L3G1, Canada*

[3]*Department of Physics, University at Buffalo, State University of New York, Buffalo, New York 14260, USA*

[4]*Department of Chemistry, University of Waterloo, Waterloo, Ontario N2L3G1, Canada*

[5]*National Institute of Standards and Technology, Gaithersburg, Maryland 20899, USA*

(Received 7 April 2026; accepted 2 October 2026; published 3 November 2026)

Coherent control of neutrons via Bragg diffraction forms the foundation of perfect crystal neutron interferometry, facilitating both fundamental tests of quantum mechanics and applications in quantum information science. In cavity geometries, perfect crystals enable neutron confinement and have been employed in precision measurements of spin-orbit interactions and for neutron electric dipole moment (nEDM) searches. However, in these conventional configurations, neutrons undergo a single pass through the crystal geometry, placing a physical constraint on both crystal and in-flight interaction times and measurement sensitivity. In this work, we introduce a neutron loop cavity that coherently recirculates neutrons through repeated Bragg reflections between perfect silicon crystal blades. This structure is predicted to achieve a neutron unitary survival probability of ∼64% for 10 000 Bragg reflections, corresponding to confinement times on the order of seconds. We propose a Schwinger interaction measurement that achieves a π spin rotation in 800 Bragg reflections, representing more than a tenfold improvement in sensitivity over recent measurements. Further applications include nEDM searches targeting the 10^{-27} e cm scale, as well as experimental tests of neutron parity violation, the neutron lifetime, and the quantum Zeno effect with neutrons.

DOI: 10.1103/vqvb-4vgw

I. INTRODUCTION

Perfect crystal neutron interferometers (NIs) have been instrumental in experimentally verifying foundational quantum phenomena [1]. Landmark experiments include the confirmation of the 4π spin rotation symmetry of spin-1/2 particles [2] and the observation of gravitationally induced phase shifts in neutron matter waves [3]. More recently, NIs have enabled studies of decoherence-free subspaces for quantum error correction [4], hypothetical fifth forces [5,6], quantum Cheshire cat and operator commutation relations [7], and neutron orbital angular momentum states [8–10].

In parallel with neutron interferometry, perfect crystal neutron cavities formed by two Bragg-diffracting silicon blades have been developed to confine and coherently control neutron beams [11–18]. These devices [see Figs. 1(a) and 1(b)] have demonstrated hundreds to thousands of Bragg reflections at high Bragg angles near 90°, extending effective interaction times and enhancing sensitivity to subtle quantum effects. This capability has enabled direct observation of neutron spin rotation from the spin-orbit interaction in silicon using ∼100 Bragg reflections [17], as well as high-precision reflectivity measurements relevant to neutron electric dipole moment (nEDM) searches, where the measured reflectivity corresponds to losses low enough to permit up to ∼20 000 reflections [18]. However, in these double Bragg neutron cavities, both crystal and in-flight interaction times are ultimately limited either by the finite device geometry, which restricts the number of achievable reflections in compact setups [17], or by practical constraints such as neutron-guide lengths, beam divergence, and alignment stability when the cavity is extended to meter scales [16]. This trade-off motivates the development of closed-loop neutron recirculation, which enables repeated passes within a compact device.

Leveraging recent advances in NI fabrication [19], demonstrated high-precision alignment of Bragg blades in split-crystal interferometers [20], and versatile dynamical diffraction modeling [21–25], we present a neutron loop cavity design that confines neutrons through a repeated four Bragg diffractions in a closed trajectory. This geometry enables controlled amplification of small, cumulative interactions. We estimate that a unitary confinement probability of approximately 64% can be achieved after 10^4 Bragg reflections, where the confinement probability is defined as the fraction of neutrons remaining in the cavity after N reflections. As a near-term application, we propose a simplified measurement of the Schwinger spin-orbit interaction, in which the looped neutron trajectory produces a π spin rotation within approximately 800 reflections. This unique setup may help

*Contact author: oalailey@uwaterloo.ca

†Contact author: dmitry.pushin@uwaterloo.ca

Published by the American Physical Society under the terms of the Creative Commons Attribution 4.0 International license. Further distribution of this work must maintain attribution to the author(s) and the published article's title, journal citation, and DOI.

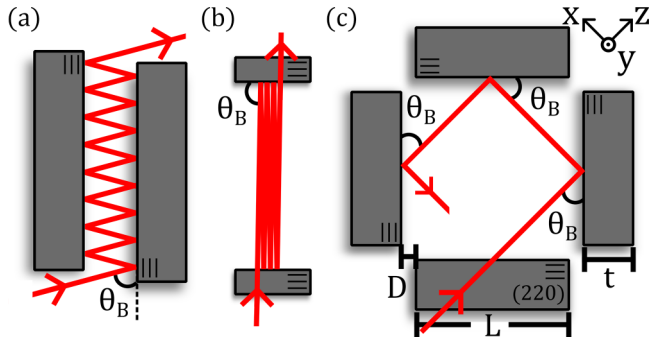


FIG. 1. Schematic of neutron propagation through three perfect crystal cavity geometries: (a) compact double Bragg blade [17,25], (b) extended double Bragg blade [16], and (c) the proposed loop cavity. In panels (a) and (b), the crystals are attached to a common base and θ_B is near 90° to maximize the number of bounces. In panel (c), the four identical Bragg blades are independently mounted and aligned to operate at $\theta_B = 45°$, confining neutrons to repeatedly traverse the same path. Note that only a few pathways of diffracted intensity are shown for simplicity.

resolve the ∼40% discrepancy between the recent experimental Schwinger measurements and theoretical predictions [17]. Furthermore, we describe how this device may be utilized for nEDM searches, neutron parity violation measurements, neutron lifetime measurements, and tests of the quantum Zeno effect with neutrons.

II. DYNAMICAL DIFFRACTION MODELING

For the design and analysis of the loop cavity, we apply the quantum information (QI) model for dynamical diffraction (DD) theory [21–25]. The QI model describes neutron propagation through perfect crystals as a quantum random walk through a lattice of nodes. Each node is a unitary operation on the neutron state that updates the neutron wavefunction at each point inside the crystals. The QI model has been shown to successfully describe the beam intensity profiles in a conventional neutron interferometer [21], as well as neutron confinement in a perfect crystal cavity composed of two Bragg blades [25] [see Fig. 1(a)]. Complete description of the model as a quantum random walk and the equivalence with DD equations can be found in Refs. [21–25].

In DD, the characteristic length scale is the *Pendellösung* length that is on the order of 50 μm [1]. As neutrons propagate through perfect crystal blades, intensity oscillates back and forth between the transmitted and reflected beams with a period equal to the *Pendellösung* length:

$$\Delta_H = \frac{\pi V_{\text{cell}}}{\lambda |F_H|} \begin{cases} \cos\theta_B & \text{Laue,} \\ \sin\theta_B & \text{Bragg,} \end{cases} \tag{1}$$

where V_{cell} is the volume of the crystal unit cell, λ is the incident neutron wavelength, F_H is the crystal structure factor, and θ_B is the Bragg angle. For $\lambda = 2.72$ Å incident on a perfect silicon crystal (220), $\theta_B \approx 45°$ and $\Delta_H \approx 40$ μm. Unless otherwise noted, these values are used for all quantities and calculations throughout the text.

Neutron storage devices that utilize Bragg diffraction exploit the fact that neutrons within a narrow angular range (or equivalently momentum) about the Bragg condition reflect with unity probability. This range of total reflection, known as the Darwin width, is given by

$$\delta\theta = \frac{|F_H|}{\pi V_{\text{cell}}} \frac{\lambda^2}{\sin(2\theta_B)}, \tag{2}$$

which gives $\delta\theta \approx 5$ μrad. The Darwin width can be nearly doubled for $\lambda = 4.4$ Å and (111), while keeping $\theta_B \approx 45°$.

III. NEUTRON LOOP CAVITY DESIGN

A schematic of the proposed loop cavity is illustrated in Fig. 1(c). Four identical Bragg blades of length L and thickness t are positioned independently in a square formation. The crystal separation distance can be increased beyond the length L by introducing a gap distance D between all crystals. Neutrons are incident upon the rightmost blade at $\theta_B = 45°$. Subsequent reflections from the blades confine the neutron to a closed, circulating trajectory. This cavity geometry requires $\theta_B = 45°$, ensuring that the reflection from one blade is incident upon the next at $90° - \theta_B = \theta_B$. Neutrons within the Darwin width about the Bragg angle are accepted and undergo repeated reflections. Similar designs have been considered for x-ray resonators [26–29]. Alignment conditions, along with experimental requirements such as crystal thickness tolerances and loading/unloading of the cavity, are discussed in Sec. III B.

A. Confined neutron wavefunction

The central purpose of a neutron cavity is to confine neutrons for an extended amount of time with a high survival probability. We analyze the propagation of the neutron wavefunction within the loop cavity as a function of the number of reflections N using the QI model. Figure 2 shows the evolution of the neutron probability intensity within the crystal blades and surrounding space for $t = 10\Delta_H$ and $L = 40\Delta_H$. Here, the simulated crystal dimensions are kept compact to clearly visualize the intensity inside the blades and within the loop. Neutrons transmit through the bottom Bragg blade without diffracting such that the first Bragg reflection will occur at the rightmost Bragg blade (discussed in loading/unloading in Sec. III B). At each subsequent coherent interaction, the transmitted component escapes, while the reflected component remains confined; four reflections constitute one complete closed loop.

Figures 2(b) and 2(c) show the neutron intensity after the second and tenth completed loops. By this stage, transmission through the Bragg crystals is negligible. This behavior is consistent with DD theory: The cavity acts as a filter, retaining only those neutrons with wavelengths within the Darwin width. For these confined neutrons, the reflectivity of the Bragg crystals is nearly unity.

This behavior is quantified in Fig. 3(a), which plots the confined intensity for up to $N = 10^4$ reflections ($t = 100\Delta_H$, $L = 2000\Delta_H$). The inset shows the deviation of the single-bounce reflectivity from unity, defined as $R(N) = I(N)/I(N-1)$, where $I(N)$ is the integrated intensity of the Nth reflected wave over the entire inner crystal face. The reflectivity follows two distinct regimes, reaching

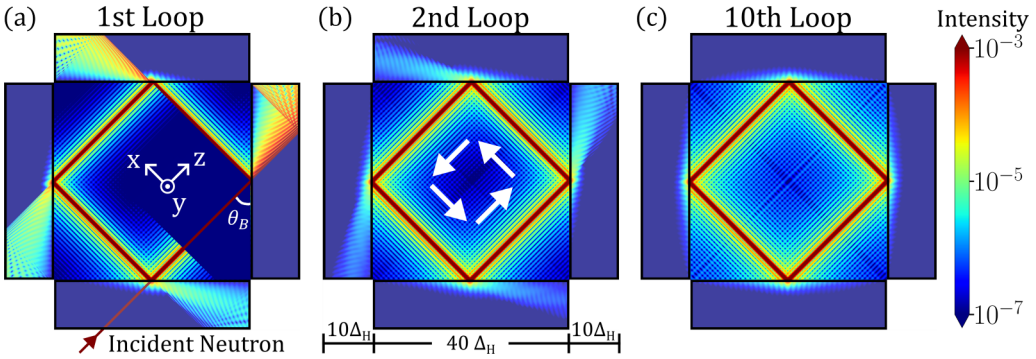


FIG. 2. (a) Simulated neutron intensity inside the loop cavity after the first four reflections. Neutrons are incident to the rightmost Bragg blade at $\theta_B = 45^\circ$, undergoing subsequent reflections in a counter clockwise direction. As the number of reflections within the loop increases [panels (b) and (c)], the neutrons within the Darwin width remain confined, with minimal intensity escaping through the crystals. In these simulations, the crystal thickness and crystal length are compact for visualization purposes.

$R(10^4) = 1 - 10^{-8}$. Initially, the escape probability $(1 - R(N))$ decreases rapidly $(\propto N^{-3})$ until a transition point $N_{\text{trans}} = 100$, which scales with the Bragg blade thickness as $N_{\text{trans}} \sim t^2$. This early behavior arises from the finite crystal thickness, which supports complex modes involving multiple internal reflections. Eventually, the dominant neutron mode stabilizes to the main reflection from the inner Bragg face. The escape probability then transitions to a shallower dependence $(\propto N^{-1})$. The cumulative survival probability is given by $P = \prod_{i=1}^{N} R(i)$. Consequently, neutrons satisfying the Bragg condition have a $P \approx 64\%$ chance of surviving 10^4 reflections.

From DD theory for successive Bragg reflections, the average reflectivity is

$$\langle R \rangle = 1 - \Delta_e n(\sigma_{\text{abs}} + \sigma_{\text{therm}}), \tag{3}$$

where Δ_e is the wavefunction extinction depth, n is the atomic density, σ_{abs} is the absorption cross section, and σ_{therm} is the diffuse scattering cross section [18]. The extinction depth, where the amplitude is reduced by e^{-1}, is defined as $\Delta_e = \sin\theta_B e^{-W}/(\lambda n b_c)$, where e^{-W} is the Debye-Waller factor and b_c is the neutron coherent scattering length for silicon. Using $e^{-W} = 0.96$, $\sigma_{\text{abs}} = 0.26$ barn, and $\sigma_{\text{therm}} = 0.161$ barn, the theoretical average reflectivity is $\langle R \rangle = 0.999\,975$. The survival fraction is then given by $\eta = \epsilon \exp^{-N(1-\langle R \rangle)}$, where $\epsilon = 0.9$ is an efficiency factor taking into account the sharp decrease in reflectivity near the edge of the Darwin plateau [18]. For $N = 10^4$ reflections, DD theory predicts a survival probability of $\eta \approx 70$ % due solely to absorption and thermal diffuse scattering. This estimate describes a distinct nonunitary loss mechanism from the coherent confinement losses captured by the QI model, and both effects contribute to the overall cavity survival probability.

Figure 3(b) shows the confined transverse intensity profile as a function of position across the inner reflecting crystal face after 10^4 reflections, resembling a sinc^2 distribution. The corresponding momentum distribution forms a rectangular pulse [Fig. 3(c)]. This agrees with DD theory, confirming that only neutrons with momenta strictly within the Darwin width survive the extended confinement. Directly related to this phenomena, we consider the neutron transverse coherence $\sigma_\perp$ as a function of the number of reflections N, where we set $\sigma_\perp$ as the first zero of the sinc^2 intensity distribution. The transverse extent rapidly saturates to 1 Δ_H according to $\sigma_\perp \sim 1 - \frac{1}{2}e^{-N/3}$.

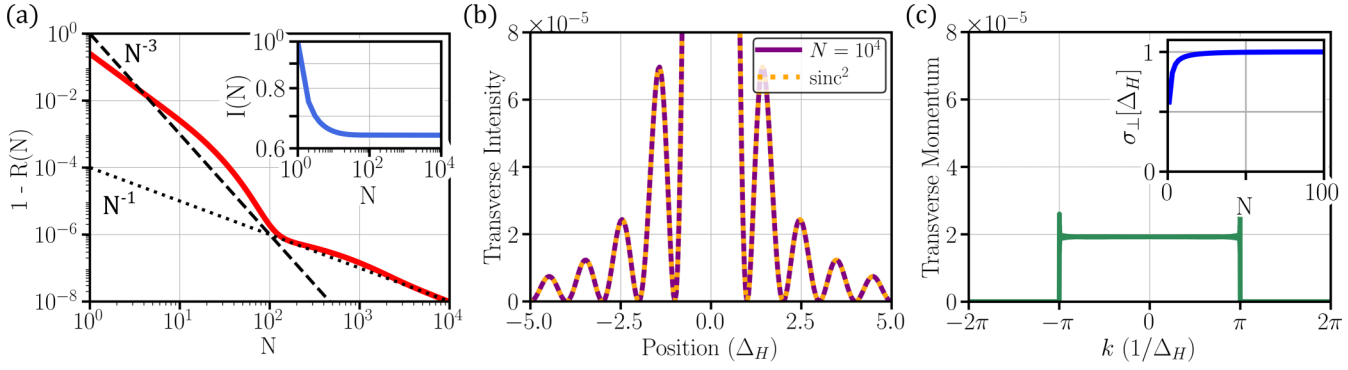


FIG. 3. Simulation of the designed cavity performance ($t = 100\Delta_H$, $L = 2000\Delta_H$). (a) The evolution of the reflectivity, plotted as $(1 - R(N))$, vs the number of reflections N. The reflectivity reaches $R = 1 - 10^{-8}$ at $N = 10^4$ reflections. The escape probability $(1 - R(N))$ follows two distinct power-law regimes: An initial rapid decay $(\propto N^{-3})$ transitioning to a shallower dependence $(\propto N^{-1})$, indicated by the dashed lines. The inset demonstrates the confined intensity $I(N)$ vs the number of reflections N. (b) Transverse intensity profile after 10^4 reflections, which is fit to a sinc^2 function. (c) Corresponding transverse momentum distribution showing the rectangular pulse characteristic of the Darwin plateau, with visible Gibbs ringing. The inset demonstrates the neutron transverse coherence $\sigma_\perp$ rapidly saturating to 1 Δ_H as a function of N, in agreement with the confined neutron momentum becoming restricted to the Darwin plateau.

B. Experimental design requirements

We outline key experimental considerations for implementing the loop cavity.

Crystal alignment. To ensure near-unity reflectivity, each Bragg blade requires alignment to each other within the Darwin width [Eq. (2)]. Consistent with established methods in neutron and x-ray optics [20,30], the crystals are mounted on piezostages for fine rotational and translational adjustment. For instance, the recently demonstrated split-crystal neutron interferometer utilized a piezo-driven tip-tilt platform achieving a $\pm 70\,\mu$rad range with subnanoradian resolution [20]. The proposed loop cavity employs independently mounted piezo-rotation stages with sub-μrad resolution and high resonant frequencies, enabling μrad-scale corrections on submillisecond timescales. Unlike split-crystal neutron interferometers, where picometre-scale relative translations and nanoradian angular stability are required to preserve two-path phase coherence [20], the loop cavity requires each crystal to remain within the Darwin acceptance of the Bragg reflection. Therefore, the alignment stability requirement is determined by the approximately 5 μrad Darwin width rather than the significantly more stringent tolerances associated with interferometric phase stability.

Furthermore, a partially monolithic implementation, where multiple crystal blades are fabricated from a single perfect crystal, represents a possible initial realization of the neutron loop cavity. Such an approach would reduce the number of independent alignment degrees of freedom and simplify the experimental demonstration of multiple Bragg reflections and neutron storage. This strategy is similar to the development of split-crystal interferometers, where the interferometer can first be characterized in a monolithic configuration before being separated and mounted on independently adjustable components. For the ultimate loop cavity geometry, independently mounted crystals provide additional flexibility by enabling control of the crystal separation and cavity dimensions, which will be important for several applications.

Loading/unloading. Several crystal gating techniques have been experimentally demonstrated in BB-type cavities for cold-neutron storage [11,16]. The task of loading/unloading is to temporarily shift incident neutrons off the Bragg condition by the Darwin width $\delta\theta$ [Eq. (2)]. Since the Bragg crystals are independently mounted on piezo-driven rotation stages for alignment, one crystal can be rotated by an angle $\delta\theta$ to load the device and subsequently returned by $-\delta\theta$, restoring the Bragg condition and confining the neutrons within the loop. For $\lambda = 2.72$ Å and a crystal length $L = 2000\Delta_H$, a neutron completes a single round trip in ∼0.15 ms. The cavity can be continuously loaded with pulses of width $\delta t = \frac{L/2+t}{\sqrt{2}v}$, where v is the neutron velocity.

For the zero-separation ($D = 0$) geometry considered here, the input crystal must therefore be rotated by approximately 5 μrad and returned and settled within ∼100 μs. Achieving this level of dynamic performance represents a significant engineering challenge. While piezo-actuated positioning systems continue to improve in bandwidth and settling time, realizing the required combination of angular precision and switching speed will likely require a dedicated actuator design. Increasing the crystal separation D increases the neutron round-trip time, thereby relaxing the required switching bandwidth, allowing the actuator performance to be optimized alongside the cavity geometry.

Another convenient option leverages the neutron's magnetic moment, which couples to a localized pulsed magnetic field, producing a Zeeman energy shift and a corresponding temporary change in the neutron wavevector while it traverses the magnetic field region:

$$\Delta k = \pm \frac{\mu B m}{\hbar^2 k}, \tag{4}$$

where μ is the neutron magnetic moment, B is the applied magnetic field, m is the neutron mass, and k is the neutron wavevector. A magnetic field pulse of approximately 3.6 T applied locally at the loading or unloading crystal produces a temporary wavevector shift equivalent to the Darwin width, enabling the neutron to transmit through the crystal. Once the neutron leaves the magnetic field region, its original wavevector is restored. Since the field is applied only during the loading and unloading events, rather than continuously during storage, the average thermal load is minimized, and the switching requirements can be further relaxed by increasing the crystal separation D, which increases the neutron round-trip time. This method provides a means of both loading and unloading neutrons into and out of the loop cavity [11].

Gravity. To maintain neutron confinement within the loop cavity, gravitational effects must be compensated. As demonstrated in other neutron storage systems [14], this can be achieved by incorporating neutron guides between the crystal blades, allowing falling neutrons to reflect from the lower guide surface with near-unity probability. In the loop cavity geometry, four neutron guides are required, one for each path segment between adjacent blades. Additionally, these guides confine the beam in the vertical direction, thereby limiting its divergence. Since the meter-long guides implemented in earlier neutron storage systems [14,16], neutron-guide technology has advanced substantially through the adoption of multilayer supermirror coatings, higher-m reflectors, and optimized guide geometries, significantly improving neutron transport efficiency and delivered flux at modern facilities [31–33]. However, the neutron guides will still introduce transport losses beyond the theoretical ∼64% confinement, which we can quantify.

For $N = 10^4$ reflections, $L = 2000\Delta_H$, $D = 0$, the total neutron path length is 570 m, corresponding to a gravitational drop of 0.75 m. For a guide height of 43 mm (as used in the cavity in Ref. [16]), this results in only approximately 17 reflections from the guide surfaces. Assuming a specular guide reflectivity of 99% [33], the corresponding transport loss is approximately 16%. The ratio of crystal blade reflections to guide reflections is approximately 500:1. For comparison, the Ref. [16] two-blade cavity geometry, depicted in Fig. 1(b), achieved approximately 2500 reflections between successive crystal blades that were 1.06 m apart. Over the corresponding 2.6 km path length, gravitational sag resulted in approximately 2000 guide reflections. The ratio of crystal blade reflections to guide reflections is approximately 1:1. Thus, guide-related losses were a dominant limitation in the Ref. [16] geometry, whereas the compact loop cavity reduces

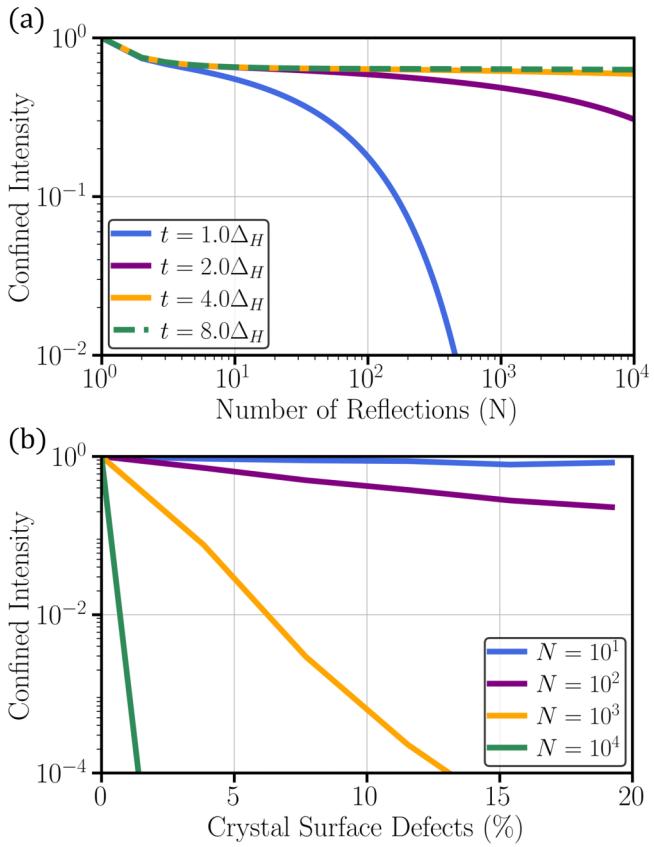


FIG. 4. (a) Confined intensity as a function of the number of reflections N for various Bragg blade thicknesses t and $L = 2000\Delta_H$. For $t < 4\Delta_H$, intensity loss increases with N, while for $t \geqslant 4\Delta_H$, confinement is maintained and does not significantly improve with further increases in thickness. (b) Confined intensity as a function of crystal blade surface roughness/defect density. Sensitivity to surface imperfections increases with the number of reflections. For up to 10^2 reflections, roughness has minimal impact, but for 10^4 reflections, crystal surfaces must be defect-free to preserve confinement.

the number of guide reflections by more than 2 orders of magnitude, relaxing the requirements on guide surface quality needed to maintain specular beam transport. For short confinement times, it may be feasible to dynamically lower the cavity, eliminating the need for guides while still accounting for the neutron free fall.

Crystal thickness and surface defects. The neutron confinement probability as a function of Bragg blade thickness t is shown in Fig. 4(a). To sustain confinement over thousands of reflections, the Bragg blades must have a thickness of at least $t \geqslant 4\Delta_H$.

Surface roughness and crystal defects are expected to limit neutron confinement [25,34]. Within the QI model, surface roughness can be incorporated by randomly replacing small regions of crystal within one Δ_H of the surface with empty space. This approach follows the methodology of Ref. [25], which modeled imperfections in an experimental BB cavity. Figure 4(b) presents the confined neutron intensity versus reflection number N for both an ideal defect-free cavity and cavities with surface roughness on the Bragg blade faces. For up to 10^2 reflections, surface roughness has little effect on confinement. At larger N, however, its impact becomes pronounced: At 10^3 reflections, a surface defect density of approximately 10% leads to substantial intensity loss, while for 10^4 reflections, perfect crystal surfaces are required to maintain confinement. This heightened sensitivity arises from the repeated interaction of the confined neutron wavefunction with the same crystal surface regions, in contrast to conventional BB cavities, where neutrons interact with each crystal surface only once.

Previous BB cavity experiments have demonstrated Bragg-blade reflectivities consistent with $\sim 2 \times 10^4$ successive crystal reflections [25]. Together with recent advances in perfect crystal fabrication, including nonetching processing techniques that have produced perfect crystal neutron interferometers with fringe contrasts exceeding 90% [19], these results suggest that the extremely low surface roughness required for neutron storage of 10^4 reflections is an achievable experimental target, although the ultimate cavity performance will require experimental verification.

IV. FUNDAMENTAL PHYSICS APPLICATIONS

Here, we discuss several potential experimental applications of the neutron loop cavity, including measurements of the neutron spin-orbit interaction, neutron electric dipole moment, nucleon-nucleon weak interaction, neutron lifetime, and neutron quantum Zeno effect. These applications can be broadly divided into two categories. The first includes promising near-term measurements, such as neutron spin-orbit interaction and quantum Zeno effect experiments, where the loop cavity geometry enables new experimental regimes through repeated neutron-crystal interactions and long effective interaction paths. The second includes precision measurements of fundamental physics observables, including the neutron electric dipole moment, nucleon-nucleon weak interaction, and neutron lifetime, where the loop cavity provides a complementary approach with distinct systematic effects and experimental capabilities, but where achieving sensitivity competitive with established techniques remains a significant challenge. For each application, we provide first-order quantitative estimates of confinement time, phase accumulation, and interaction strength, together with comparisons to existing experimental approaches where applicable. Detailed systematic studies will require experimental construction and characterization of the neutron loop cavity; however, this analysis establishes both the potential opportunities and primary limitations of the loop cavity.

Considering practical cold, monochromatic neutron beams with flux on the order of 10^5 n/(cm^2 s), a beam size of 1 cm^2 corresponds to an incident rate of 10^5 neutrons/s at the cavity entrance. For a beam divergence of 1 mrad and a Darwin width of 5 μrad, only an approximate fraction $\sim 5 \times 10^{-3}$ of the incident neutrons are accepted, yielding a rate of 500 neutrons/s. As discussed in Sec. III, the survival probability after 10^4 reflections is approximately 64%, corresponding to ~300 neutrons/s exiting the cavity and reaching the detector. Accounting for additional reductions due to crystal misalignment, neutron transport losses, timing inefficiencies in loading and unloading, and the inclusion of spin polarizers and

analyzers, the expected detected count rate is conservatively on the order of 1–10 Hz.

A. Neutron spin-orbit interaction and nEDM

The neutron spin-orbit interaction, or Schwinger scattering, induces a small spin rotation of the neutron due to the coupling of its magnetic dipole moment (MDM) with the atomic electric field during a single Bragg reflection [35,36]. This interaction has been utilized in past efforts to search for the nEDM using Bragg reflection from perfect crystals [37]. More recently, the Schwinger interaction in noncentrosymmetric perfect crystals has been experimentally explored as a basis for nEDM measurements [38–40]. To enhance sensitivity to either the spin-orbit interaction or the nEDM in Bragg scattering, several techniques have been proposed that involve hundreds to thousands of Bragg reflections within slotted crystals to increase the neutron's interaction time with the internal electric field [17,18,41]. The loop cavity enables orders-of-magnitude improvement in the interaction time, along with other practical advantages, potentially enabling higher-sensitivity Schwinger and nEDM measurements.

The motion of a neutron through the atomic electric field $\vec{E}$ induces an effective magnetic field in the neutron rest frame:

$$\vec{B}_{\text{eff}} = \frac{1}{c}\vec{v} \times \vec{E}, \tag{5}$$

where c is the speed of light and $\vec{v}$ is the neutron velocity. In this field, a neutron with spin polarization $\vec{P}$ will rotate around $\vec{B}_{\text{eff}}$ due to the torque on the MDM:

$$\vec{\tau}_{\text{MDM}} = \mu_n \vec{P} \times \vec{B}_{\text{eff}}, \tag{6}$$

where μ_n is the nuclear magnetic moment. The expected magnitude of rotation for a single Bragg reflection is approximately

$$\theta_i = 2|b_{\text{so}}/b_c|, \tag{7}$$

where b_{so} is the Schwinger scattering length and $b_c = 0.415 \times 10^{-12}$ cm is the coherent nuclear scattering length for silicon. For $\theta_B = 85^\circ$ and (220) Bragg reflection used in Ref. [17], the rotation angle is $\theta_i = 3.27 \times 10^{-4}$ rad. By employing a slotted crystal, 136 reflections were achieved, magnifying the spin rotation to a measured 4.73×10^{-2} rad. Notably, for the Schwinger rotation to add constructively in the BB geometry, the entire crystal was placed in a uniform magnetic field such that the neutron spin undergoes a precession of angle π between successive Bragg reflections from opposing crystal faces. In the absence of this condition, the Schwinger spin rotation does not accumulate with each reflection as the effective magnetic field $\vec{B}_{\text{eff}}$ reverses sign at each reflection. In Ref. [17], the measured spin rotation was 40% larger than expected, indicating a need for further characterization of the Schwinger interaction with an improved setup.

The loop cavity geometry supports a large number of Bragg reflections without requiring the high Bragg angles characteristic of slotted crystal designs. For the (220) reflection at $\theta_B = 45^\circ$, the Schwinger rotation per reflection is $\theta_i = 3.96 \times 10^{-3}$ rad, representing an order-of-magnitude enhancement compared to standard configurations. Moreover, the condition for constructive accumulation of the Schwinger rotation is simplified due to the loop geometry. The 90° rotational symmetry of the cavity ensures that $\vec{v} \times \vec{E}$ points in the same direction for each Bragg reflection. Consequently, the effective magnetic field $\vec{B}_{\text{eff}}$ has the same orientation at every Bragg blade. This contrasts with double-Bragg cavities, where $\vec{B}_{\text{eff}}$ reverses sign between reflections [17]. A guide field, however, is still required to preserve the neutron polarization: It maintains the polarization along $(x+z)/\sqrt{2}$ throughout the device (see Fig. 2) and should be tuned to avoid partial cancellation as the spin precesses between reflections. The accumulated spin rotation reaches 0.54 rad after 136 reflections and a full π rad after 800 reflections, nearly 100 times larger than previous measurements [17].

TABLE I. Estimated neutron EDM statistical sensitivity comparison.

Technique	E (V/cm)	T (s)	N	$ET\sqrt{N}$
UCN [42]	1.1×10^4	180	1.1×10^4	2×10^8
Loop cavity	1×10^9	2×10^{-3}	10	6×10^6

In Ref. [18], a slotted crystal with reflectivity $R \geqslant 0.999\,98$ was reported, possibly enabling tens of thousands of bounces. The authors estimated that by coupling the neutron EDM to the atomic electric field at each Bragg reflection [37] a sensitivity of order 10^{-27} e cm could be achievable, potentially surpassing the current experimental constraint $d_n = (0.0 \pm 1.1_{\text{stat}} \pm 0.2_{\text{sys}}) \times 10^{-26}$ e cm [42]. For any nEDM measurement, the statistical sensitivity is proportional to the product $E\tau N^{1/2}$, where E is the electric field, τ is the interaction time, and N is the number of counted neutrons [43].

Shown in Table I is a comparison of the estimated statistical sensitivity of the neutron loop cavity with the current experimental constraint obtained using ultracold neutrons (UCN) [42]. For the loop cavity estimate, we consider 10^4 Bragg reflections, with each individual crystal interaction contributing an electric-field interaction time of 0.2 μs [43]. Additionally, we assume a conservative survival probability such that only 10 neutrons remain after 10^4 reflections. Under these assumptions, the loop cavity sensitivity is approximately 1.5 orders of magnitude below the current UCN limit. Nevertheless, the loop cavity approach provides a complementary measurement technique with distinct systematic effects, with significant potential for improved sensitivity through longer storage times and enhanced neutron storage efficiency, thereby increasing both the accumulated interaction time and the detected neutron count.

B. Parity violation with liquid helium-4

The nucleon-nucleon (NN) weak interaction remains a poorly constrained sector of the standard model [44]. Parity violation (PV) serves as a unique filter to isolate the weak force from the dominant, parity-conserving strong interaction, which typically suppresses PV amplitudes by a factor of 10^{-6} to 10^{-7}. To theoretically interpret these effects, few-nucleon systems, such as with neutrons, are essential; they allow a straightforward mapping between experimental observables and underlying NN interactions [44]. In liquid helium-4, this interaction manifests as a rotation of

the neutron spin about its momentum vector, theoretically predicted to be on the order of 10^{-6} to 10^{-7} rad/m. The current best experimental limit, $d\phi/dz = [+1.7 \pm 9.1(\text{stat}) \pm 1.4(\text{sys})] \times 10^{-7}$ rad/m [45], is dominated by large statistical uncertainties.

The loop cavity enables optimal ^{4}He interaction lengths to maximize the signal-to-noise scaling, while simultaneously utilizing a simplified sample environment and distinct systematic controls. In Ref. [45], two 0.42 m liquid ^{4}He targets were alternately filled, with a π spin flipper placed between them, in order to isolate the PV neutron spin rotation signal. The use of long targets is motivated by the linear scaling of the PV rotation angle, $\phi \propto \rho z$, with number density of scatterers ρ and target length z. However, for transmission experiments, the statistical uncertainty $\propto\sqrt{e^{-\rho\sigma_{\text{tot}}z}}$ is minimized when the target length equals twice the neutron mean free path, $z = 2/(\rho\sigma_{\text{tot}})$, where σ_{tot} is the total scattering cross section. For liquid ^{4}He at the cold-neutron energies used in the experiment, this optimal length is approximately 2 m; however, only 0.42 m targets were used due to the 100 cm maximum bore length of the cryostat [46]. Achieving an effective interaction length near 2 m would therefore yield a 2× gain in sensitivity. In the loop cavity, this condition can be met by repeatedly circulating neutrons through a much shorter target; for example, a 1 cm liquid ^{4}He sample traversed 200 times yields an effective path length of 2 m. A significant limitation is the narrow phase-space acceptance of the crystal cavity, which results in a substantially lower neutron count rate than the intense polychromatic flux (10^7 n/cm^2 s) used in Ref. [46]. Consequently, the statistical sensitivity is expected to be orders of magnitude lower. Nevertheless, the simplified and compact interaction geometry, together with new opportunities for systematic background suppression, may still enable a complementary measurement with certain experimental advantages.

Specifically, this architecture enables more direct control over parity-conserving backgrounds without relying on complex sample manipulation. In Ref. [45], background subtraction required alternately filling and draining two liquid ^{4}He target chambers with a π spin flipper placed between them in order to isolate the PV neutron spin rotation signal. In the loop cavity, however, the sign of the PV spin rotation may be reversed by rotating the entire cavity by 90° about the entrance crystal, which reverses the neutron propagation direction through the loop from counterclockwise to clockwise. This transformation flips the neutron momentum at the target location, $\mathbf{k} \to -\mathbf{k}$. Since the PV rotation changes sign under $\mathbf{k} \to -\mathbf{k}$, while many parity-conserving magnetic backgrounds do not, the PV signal may be isolated without modifying the target configuration or requiring a spin flipper.

C. Neutron lifetime

The "neutron lifetime puzzle" remains an active area of research [47–49], with the mean neutron lifetime τ_n a key input parameter for models of the early universe [50]. Two main experimental approaches are used, with ongoing disagreement at the ∼1% level. The beam method primarily measures the rate of proton production from neutron beta decay in a cold-neutron beam,

$$n \to p + e^- + \overline{\nu_e}, \tag{8}$$

while the bottle method measures the survival of stored ultracold neutrons as a function of time. A neutron lifetime measurement using a loop cavity would fall under the bottle method, but with neutron energies ∼10^5× larger (comparable to beam experiments) and a fundamentally different experimental geometry. Furthermore, the cold-neutron flux is many orders of magnitude higher than that available for ultracold neutrons, making the loop cavity a unique variant of a bottle-type experiment.

Neutrons are loaded into the loop, stored for a variable time Δt, and then extracted and counted. The measured quantity is the number of surviving neutrons $N(\Delta t)$. In addition to beta decay, neutrons are lost through imperfect reflections from the crystal mirrors. This is a well-known issue in bottle experiments and is typically addressed by varying the trap geometry to change the collision rate. Extrapolating to zero collision rate allows the decay lifetime to be extracted. In the loop cavity, this can be achieved by changing the separation D between independently mounted crystals, which increases the path length and reduces the reflection rate.

The feasibility of the loop cavity depends on whether neutrons can be confined for times comparable to or exceeding $\tau_n \approx 15$ min. For a loop length $L = 2000\Delta_H$ (and $D = 0$), a neutron completes one circuit in approximately 0.15 ms. Over 15 min, this corresponds to roughly 6×10^6 Bragg reflections, requiring reflectivity $R > 1 - 10^{-6}$ for confinement. In the ideal unitary simulations shown in Fig. 3(a), reflectivities approaching $R = 1 - 10^{-8}$ are obtained when absorption and thermal scattering are neglected. Experimentally, however, reflectivities of $R = 1 - 2 \times 10^{-5}$ have been reported for slotted silicon crystals [18], corresponding to confinement times on the order of seconds. Increasing the crystal separation D reduces the required number of Bragg reflections by increasing the transit time between reflections, but this introduces longer neutron transport paths where finite guide reflectivity becomes a major source of loss [16]. Consequently, with current crystal and neutron-guide technology, confinement for durations approaching the neutron lifetime does not appear feasible. Nevertheless, storage times on the order of 1 min would still result in approximately 7% of the stored neutrons decaying via beta decay while reducing the required number of crystal reflections by more than an order of magnitude. Although such measurements would not be statistically competitive with dedicated neutron lifetime experiments, they would constitute the first proof-of-principle demonstration of a bottle-type lifetime measurement using beam-energy neutrons and would provide a valuable characterization of the achievable storage performance and associated systematic effects of the loop cavity.

D. Quantum Zeno effect and Zeno dragging

The quantum Zeno effect (QZE) is a fundamental prediction of quantum mechanics: Frequent measurements can suppress the coherent time evolution of a quantum system [51,52]. It has been demonstrated in many physical systems [52–54], but has yet to be observed with neutrons due to

the experimental complexity of existing proposals [16,55–57]. The loop cavity provides a simple and controlled platform to test the QZE with neutrons and also enables the related concept of quantum Zeno dragging, which has applications in quantum control [58,59].

To illustrate the QZE for neutrons, consider a neutron initially in the spin-up state (↑) polarized along the z axis, passing through a magnetic field oriented along the transverse x axis (see Fig. 2) over a length l. The probability that the neutron remains in the spin-up state after the interaction is

$$P_{\uparrow} = \cos^2\left(\frac{\omega_L l}{2v}\right), \tag{9}$$

where ω_L is the Larmor frequency and v is the neutron velocity. If the interaction region is divided into N_Z segments and a spin measurement is performed after each segment, the survival probability becomes

$$P_{\uparrow}^{(N_Z)} = \cos^{2N_Z}\left(\frac{\omega_L l}{2N_Z v}\right) \xrightarrow{N_Z\to\infty} 1, \tag{10}$$

demonstrating the quantum Zeno effect. Neutron spin measurements can be implemented using polarized ^{3}He cells, which transmit one spin state while absorbing the opposite state [60]. Typical ^{3}He cell polarization can reach about 85%.

The loop cavity naturally realizes this repeated-measurement limit. A neutron circulating in the loop passes through the same magnetic field and spin analyzer on every round trip, with the number of loops equaling N_Z. Only a single magnetic field region and a single ^{3}He cell are required. A small DC coil placed in one arm of the loop produces a transverse magnetic field, as commonly used in neutron interferometry [61]. For example, a 0.1 mT field over 2.5 cm produces a total π spin rotation after approximately ten loops, which can be verified by unloading the neutrons and analyzing their spin with a second polarized ^{3}He cell outside the cavity.

To observe the QZE, a polarized ^{3}He cell is added to the opposite arm of the loop, with its polarization aligned along the beam direction. Cells a few centimeters in size have been successfully integrated into neutron interferometers before [62,63]. With the spin measurement every loop, QZE predicts that the neutron spin remains frozen in the initial ↑ state, in contrast to the full spin flip observed when only the magnetic field is present. Comparing these two configurations provides a direct test of the QZE with polarized neutrons.

Quantum Zeno dragging uses the same measurement-induced dynamics to coherently steer the quantum state. Consider again a neutron prepared in the ↑ state, circulating in the loop with only a polarized ^{3}He cell present. If the polarization axis of the cell is rotated by a small angle $\delta\theta$ between successive loops, the neutron is projected onto a slightly rotated spin state. After N_Z loops, the spin follows the measurement axis, achieving a total rotation of $N_Z\delta\theta$. For $\delta\theta = 1$ mrad, a π rotation is reached after approximately 3000 loops. Unloading the neutrons and analyzing the spin demonstrates that the spin has been coherently dragged from ↑ to ↓. This mechanism is closely related to adiabatic spin rotation, but is driven purely by measurement [64].

V. CONCLUSION

We have designed and modeled a neutron loop cavity that coherently guides neutrons through a repeated closed-loop path via Bragg diffraction from perfect crystals. We estimate a unitary confinement probability of ∼64% for 10 000 reflections, enabling precision studies of small interactions amplified by repeated traversal of the same interaction region.

As a near-term application, we propose a next-generation neutron spin-orbit interaction measurement capable of producing a π spin rotation within approximately 800 loop passes. This represents an order-of-magnitude improvement in sensitivity compared to recent measurements [17]. Moreover, an independent determination of this effect may help clarify the ∼40% discrepancy between experimental results and theoretical predictions for the spin rotation magnitude. Relative to earlier nEDM studies using slotted crystals [18], the loop cavity may enable a substantially increased effective interaction time. This enhancement suggests a path toward future nEDM searches with target sensitivity at the competitive 10^{-27}e cm level.

The loop cavity is also well suited for a first experimental test of the quantum Zeno effect with cold neutrons, using experimentally practical crystal sizes, magnetic field strengths, and polarized ^{3}He spin filters. In addition, the cavity geometry enables parity-violating measurements with ∼100× smaller samples, while offering experimental systematics distinct from existing approaches. The loop cavity further provides a novel bottle-type geometry for neutron lifetime studies at distinct energy scales, contributing an independent data point toward resolving the neutron lifetime discrepancy.

Beyond the applications presented in this work, the neutron loop cavity offers a flexible experimental platform for exploring a range of fundamental quantum phenomena. The Aharonov-Casher effect, in which a magnetic dipole acquires a topological phase when encircling a charged electrode [65], is a natural target due to the large phase amplification achievable through repeated loop traversal. This effect was previously measured using neutron interferometry, though a scaling factor of ∼1.5× was required to reconcile experiment and theory [66]. The cavity may also provide a controlled platform for studying fermionic quantum statistics. For non-interacting neutrons, the Pauli exclusion principle leads to fermion antibunching, which has been predicted and observed in thermal neutron beams [67–70]. Antibunching should place fundamental limits on the number of neutrons that can be simultaneously confined in the cavity.

ACKNOWLEDGMENTS

This work was supported by the Canadian Excellence Research Chairs (CERC) program, the Natural Sciences and Engineering Research Council of Canada (NSERC) Discovery program, the NSERC Canada Graduate Scholarships programs (CGS-M and PGS-D), Collaborative Research and Training Experience (CREATE) program, the Canada First

Research Excellence Fund (CFREF), and the U.S. Department of Energy, Office of Nuclear Physics, under Interagency Agreement No. 89243019SSC000025. D.A.P and M.G.H are grateful for discussions with Muhammad Arif.

DATA AVAILABILITY

The data that support the findings of this article are openly available [71,72].

[1] H. Rauch and S. A. Werner, *Neutron Interferometry: Lessons in Experimental Quantum Mechanics, Wave-Particle Duality, and Entanglement*, 2nd ed. (Oxford University Press, Oxford, 2015), Vol. 12.

[2] H. Rauch, A. Zeilinger, G. Badurek, A. Wilfing, W. Bauspiess, and U. Bonse, Verification of coherent spinor rotation of fermions, Phys. Lett. A **54**, 425 (1975).

[3] R. Colella, A. W. Overhauser, and S. A. Werner, Observation of gravitationally induced quantum interference, Phys. Rev. Lett. **34**, 1472 (1975).

[4] D. A. Pushin, M. G. Huber, M. Arif, and D. G. Cory, Experimental realization of decoherence-free subspace in neutron interferometry, Phys. Rev. Lett. **107**, 150401 (2011).

[5] K. Li, M. Arif, D. G. Cory, R. Haun, B. Heacock, M. G. Huber, J. Nsofini, D. A. Pushin, P. Saggu, D. Sarenac, *et al.*, Neutron limit on the strongly-coupled chameleon field, Phys. Rev. D **93**, 062001 (2016).

[6] B. Heacock, T. Fujiie, R. W. Haun, A. Henins, K. Hirota, T. Hosobata, M. G. Huber, M. Kitaguchi, D. A. Pushin, H. Shimizu, M. Takeda, R. Valdillez, Y. Yamagata, and A. R. Young, Pendellösung interferometry probes the neutron charge radius, lattice dynamics, and fifth forces, Science **373**, 1239 (2021).

[7] A. Danner, H. Lemmel, R. Wagner, S. Sponar, and Y. Hasegawa, Neutron interferometer experiments studying fundamental features of quantum mechanics, Atoms **11**, 98 (2023).

[8] C. W. Clark, R. Barankov, M. G. Huber, M. Arif, D. G. Cory, and D. A. Pushin, Controlling neutron orbital angular momentum, Nature (London) **525**, 504 (2015).

[9] D. Sarenac, M. G. Huber, B. Heacock, M. Arif, C. W. Clark, D. G. Cory, C. B. Shahi, and D. A. Pushin, Holography with a neutron interferometer, Opt. Express **24**, 22528 (2016).

[10] N. Geerits, H. Lemmel, A.-S. Berger, and S. Sponar, Phase vortex lattices in neutron interferometry, Commun. Phys. **6**, 209 (2023).

[11] M. Schuster, H. Rauch, E. Seidl, E. Jericha, and C. Carlile, Test of a perfect crystal neutron storage device, Phys. Lett. A **144**, 297 (1990).

[12] M. Schuster, E. Jericha, C. Carlile, and H. Rauch, A cold neutron storage device and a neutron resonator, Phys. B: Condens. Matter **180–181**, 997 (1992).

[13] E. Jericha, C. Carlile, and H. Rauch, Performance of an improved perfect crystal neutron storage cavity, Nucl. Instrum. Methods Phys. Res. Sect. A **379**, 330 (1996).

[14] E. Jericha, C. Carlile, M. Jäkel, and H. Rauch, Cold neutron storage by perfect crystals, Phys. B: Condens. Matter **234–236**, 1066 (1997).

[15] M. R. Jaekel, C. J. Carlile, E. Jericha, D. E. Schwab, and H. Rauch, New measurements with a perfect crystal cavity for neutrons, in *EUV, X-Ray, and Neutron Optics and Sources*, Proceedings of SPIE Vol. 3767 (SPIE, Bellingham, WA, 1999), pp. 353–359.

[16] M. Jaekel, E. Jericha, and H. Rauch, New developments in cold neutron storage with perfect crystals, Nucl. Instrum. Methods Phys. Res. Sect. A **539**, 335 (2005).

[17] T. R. Gentile, M. G. Huber, D. D. Koetke, M. Peshkin, M. Arif, T. Dombeck, D. S. Hussey, D. L. Jacobson, P. Nord, D. A. Pushin, and R. Smither, Direct observation of neutron spin rotation in Bragg scattering due to the spin-orbit interaction in silicon, Phys. Rev. C **100**, 034005 (2019).

[18] T. Dombeck, R. Ringo, D. D. Koetke, H. Kaiser, K. Schoen, S. A. Werner, and D. Dombeck, Measurement of the neutron reflectivity for Bragg reflections off a perfect silicon crystal, Phys. Rev. A **64**, 053607 (2001).

[19] M. Huber, B. Heacock, I. Taminiau, D. G. Cory, D. Sarenac, R. Valdillez, and D. A. Pushin, Achieving a near-ideal silicon crystal neutron interferometer using submicrometer fabrication techniques, Phys. Rev. Res. **6**, 043079 (2024).

[20] H. Lemmel, M. Jentschel, H. Abele, F. Lafont, B. Guerard, C. P. Sasso, G. Mana, and E. Massa, Neutron interference from a split-crystal interferometer, J. Appl. Crystallogr. **55**, 870 (2022).

[21] J. Nsofini, K. Ghofrani, D. Sarenac, D. G. Cory, and D. A. Pushin, Quantum-information approach to dynamical diffraction theory, Phys. Rev. A **94**, 6 (2016).

[22] J. Nsofini, D. Sarenac, K. Ghofrani, M. G. Huber, M. Arif, D. G. Cory, and D. A. Pushin, Noise refocusing in a five-blade neutron interferometer, J. Appl. Phys. **122**, 054501 (2017).

[23] J. Nsofini, D. Sarenac, D. G. Cory, and D. A. Pushin, Coherence optimization in neutron interferometry through defocusing, Phys. Rev. A **99**, 043614 (2019).

[24] O. Nahman-Lévesque, D. Sarenac, D. G. Cory, B. Heacock, M. G. Huber, and D. A. Pushin, Generalizing the quantum information model for dynamic diffraction, Phys. Rev. A **105**, 022403 (2022).

[25] O. Nahman-Lévesque, D. Sarenac, O. Lailey, D. G. Cory, M. G. Huber, and D. A. Pushin, Quantum information approach to the implementation of a neutron cavity, New J. Phys. **25**, 073016 (2023).

[26] W. Bond, M. Duguay, and P. Rentzepis, Proposed resonator for an x-ray laser, Appl. Phys. Lett. **10**, 216 (1967).

[27] R. D. Deslattes, X-ray monochromators and resonators from single crystals, Appl. Phys. Lett. **12**, 133 (1968).

[28] R. Cotterill, A universal planar x-ray resonator, Appl. Phys. Lett. **12**, 403 (1968).

[29] P. Liu, P. Pradhan, X. Shi, D. Shu, K. Kauchha, Z. Qiao, K. Tamasaku, T. Osaka, D. Zhu, T. Sato, J. MacArthur, X. Huang, L. Assoufid, M. White, K.-J. Kim, and Y. Shvyd'ko, X-ray optics for the cavity-based x-ray free-electron laser, J. Synchrotron Radiat. **31**, 751 (2024).

[30] U. Bonse and E. te Kaat, A two-crystal x-ray interferometer, Z. Phys. **214**, 16 (1968).

[31] M. D. Le, T. Guidi, R. Bewley, J. R. Stewart, E. M. Schooneveld, D. Raspino, D. E. Pooley, J. Boxall, K. F. Gascoyne, N. J. Rhodes, S. R. Moorby, D. J. Templeman, L. C. Afford, S. P. Waller, D. Zacek, and R. C. R. Shaw, Upgrade of

the MARI spectrometer at ISIS, Nucl. Instrum. Methods Phys. Res. Sect. A **1056**, 168646 (2023).

[32] National Institute of Standards and Technology, NCNR guide upgrade, NIST Center for Neutron Research, 2026, https://www.nist.gov/ncnr/facilities-upgrades-during-unplanned-outage/ncnr-guide-upgrade.

[33] H. Abele, D. Dubbers, H. Häse, M. Klein, A. Knöpfler, M. Kreuz, T. Lauer, B. Märkisch, D. Mund, V. Nesvizhevsky, A. Petoukhov, C. Schmidt, M. Schumann, and T. Soldner, Characterization of a ballistic supermirror neutron guide, Nucl. Instrum. Methods Phys. Res. Sect. A **562**, 407 (2006).

[34] A. Authier, S. Lagomarsino, and B. K. Tanner, *X-ray and Neutron Dynamical Diffraction: Theory and Applications* (Springer Science & Business Media, New York, 2012), Vol. 357.

[35] J. Schwinger, On the polarization of fast neutrons, Phys. Rev. **73**, 407 (1948).

[36] C. Shull, Neutron spin-neutron orbit interaction with slow neutrons, Phys. Rev. Lett. **10**, 297 (1963).

[37] C. Shull and R. Nathans, Search for a neutron electric dipole moment by a scattering experiment, Phys. Rev. Lett. **19**, 384 (1967).

[38] V. Fedorov, I. Kuznetsov, E. Lapin, S. Y. Semenikhin, and V. Voronin, Neutron spin optics in noncentrosymmetric crystals as a new way for nEDM search, Nucl. Instrum. Methods Phys. Res. Sect. B **252**, 131 (2006).

[39] V. V. Fedorov, M. Jentschel, I. A. Kuznetsov, E. G. Lapin, E. Lelièvre-Berna, V. Nesvizhevsky, A. Petoukhov, S. Yu. Semenikhin, T. Soldner, V. V. Voronin, and Y. P. Braginetz, Measurement of the neutron electric dipole moment via spin rotation in a non-centrosymmetric crystal, Phys. Lett. B **694**, 22 (2010).

[40] V. Fedorov and V. Voronin, Modern status of searches for nEDM, using neutron optics and diffraction in noncentrosymmetric crystals, in *Proceedings of the International Conference on Neutron Optics (NOP2017)*, JPS Conference Proceedings Vol. 22 (Physical Society of Japan, Tokyo, 2018), p. 011007.

[41] A. Zeilinger, M. A. Horne, and H. J. Bernstein, Symmetry violations and Schwinger scattering in neutron interferometry, J. Phys. Colloq. **45**, C3-209 (1984).

[42] C. Abel, S. Afach, N. J. Ayres, C. A. Baker, G. Ban, G. Bison, K. Bodek, V. Bondar, M. Burghoff, E. Chanel, *et al.*, Measurement of the permanent electric dipole moment of the neutron, Phys. Rev. Lett. **124**, 081803 (2020).

[43] S. Lamoreaux and R. Golub, Experimental searches for the neutron electric dipole moment, J. Phys. G: Nucl. Part. Phys. **36**, 104002 (2009).

[44] M. R. Schindler and R. P. Springer, The theory of parity violation in few-nucleon systems, Prog. Part. Nucl. Phys. **72**, 1 (2013).

[45] W. M. Snow, C. D. Bass, T. D. Bass, B. E. Crawford, K. Gan, B. R. Heckel, D. Luo, D. M. Markoff, A. M. Micherdzinska, H. P. Mumm, J. S. Nico, A. K. Opper, M. Sarsour, E. I. Sharapov, H. E. Swanson, S. B. Walbridge, and V. Zhumabekova, Upper bound on parity-violating neutron spin rotation in ^{4}He, Phys. Rev. C **83**, 022501 (2011).

[46] C. D. Bass, T. D. Bass, B. Heckel, C. Huffer, D. Luo, D. Markoff, A. Micherdzinska, W. Snow, H. Swanson, and S. Walbridge, A liquid helium target system for a measurement of parity violation in neutron spin rotation, Nucl. Instrum. Methods Phys. Res. Sect. A **612**, 69 (2009).

[47] R. Musedinovic, L. S. Blokland, C. B. Cude-Woods, M. Singh, M. A. Blatnik, N. Callahan, J. H. Choi, S. M. Clayton, B. W. Filippone, W. R. Fox, *et al.*, Measurement of the free neutron lifetime in a magneto-gravitational trap with *in situ* detection, Phys. Rev. C **111**, 045501 (2025).

[48] J. Caylor, R. Biswas, B. Crawford, M. S. Dewey, N. Fomin, G. L. Greene, S. F. Hoogerheide, J. Hungria-Negron, H. P. Mumm, J. S. Nico, F. E. Wietfeldt, D. O. Valete, and J. Zuchegno, Detection of molecular hydrogen in a neutron beam lifetime experiment, Phys. Rev. C **112**, 065501 (2025).

[49] Y. Fuwa, T. Hasegawa, K. Hirota, T. Hoshino, R. Hosokawa, G. Ichikawa, S. Ieki, T. Ino, Y. Iwashita, M. Kitaguchi, *et al.*, Improved measurements of neutron lifetime with cold neutron beam at J-PARC, arXiv:2412.19519.

[50] T. Chowdhury and S. Ipek, Neutron lifetime anomaly and Big Bang nucleosynthesis, Can. J. Phys. **102**, 96 (2024).

[51] B. Misra and E. G. Sudarshan, The Zeno's paradox in quantum theory, J. Math. Phys. **18**, 756 (1977).

[52] W. M. Itano, D. J. Heinzen, J. J. Bollinger, and D. J. Wineland, Quantum Zeno effect, Phys. Rev. A **41**, 2295 (1990).

[53] M. C. Fischer, B. Gutiérrez-Medina, and M. G. Raizen, Observation of the quantum Zeno and anti-Zeno effects in an unstable system, Phys. Rev. Lett. **87**, 040402 (2001).

[54] P. Kwiat, H. Weinfurter, T. Herzog, A. Zeilinger, and M. A. Kasevich, Interaction-free measurement, Phys. Rev. Lett. **74**, 4763 (1995).

[55] S. Pascazio, M. Namiki, G. Badurek, and H. Rauch, Quantum Zeno effect with neutron spin, Phys. Lett. A **179**, 155 (1993).

[56] H. Rauch, Quantum Zeno-effect with polarized neutrons, Phys. B: Condens. Matter **297**, 299 (2001).

[57] P. Facchi, Y. Nakaguro, H. Nakazato, S. Pascazio, M. Unoki, and K. Yuasa, Optimization of a neutron-spin test of the quantum Zeno effect, Phys. Rev. A **68**, 012107 (2003).

[58] P. Lewalle, Y. Zhang, and K. B. Whaley, Optimal Zeno dragging for quantum control: A shortcut to Zeno with action-based scheduling optimization, PRX Quantum **5**, 020366 (2024).

[59] S. Hacohen-Gourgy, L. P. García-Pintos, L. S. Martin, J. Dressel, and I. Siddiqi, Incoherent qubit control using the quantum Zeno effect, Phys. Rev. Lett. **120**, 020505 (2018).

[60] T. R. Gentile, P. Nacher, B. Saam, and T. G. Walker, Optically polarized He_3, Rev. Mod. Phys. **89**, 045004 (2017).

[61] S. A. Werner, R. Colella, A. W. Overhauser, and C. Eagen, Observation of the phase shift of a neutron due to precession in a magnetic field, Phys. Rev. Lett. **35**, 1053 (1975).

[62] M. G. Huber, M. Arif, T. C. Black, W. C. Chen, T. R. Gentile, D. S. Hussey, D. A. Pushin, F. E. Wietfeldt, and L. Yang, Precision measurement of the $n-{}^3$He incoherent scattering length using neutron interferometry, Phys. Rev. Lett. **102**, 200401 (2009).

[63] M. G. Huber, M. Arif, W. C. Chen, T. R. Gentile, D. S. Hussey, T. C. Black, D. A. Pushin, C. B. Shahi, F. E. Wietfeldt, and L. Yang, Neutron interferometric measurement of the scattering length difference between the triplet and singlet, Phys. Rev. C **90**, 064004 (2014).

[64] D. Burgarth, P. Facchi, G. Gramegna, and K. Yuasa, One bound to rule them all: From adiabatic to Zeno, Quantum **6**, 737 (2022).

[65] Y. Aharonov and A. Casher, Topological quantum effects for neutral particles, Phys. Rev. Lett. **53**, 319 (1984).

[66] A. Cimmino, G. I. Opat, A. G. Klein, S. A. Werner, S. Werner, M. Arif, and R. Clothier, Observation of the topological Aharonov-Casher phase shift by neutron interferometry, Phys. Rev. Lett. **63**, 380 (1989).

[67] S. Boffi and G. Caglioti, Further remarks on the coherence properties of a thermal neutron beam, Nuov. Cim. B **3**, 262 (1971).

[68] M. Silverman, On the feasibility of a neutron Hanbury Brown—Twiss experiment with gravitationally-induced phase shift, Phys. Lett. A **132**, 154 (1988).

[69] M. Iannuzzi, A. Orecchini, F. Sacchetti, P. Facchi, and S. Pascazio, Direct experimental evidence of free-fermion antibunching, Phys. Rev. Lett. **96**, 080402 (2006).

[70] M. Iannuzzi, R. Messi, D. Moricciani, A. Orecchini, F. Sacchetti, P. Facchi, and S. Pascazio, Further evidence of antibunching of two coherent beams of fermions, Phys. Rev. A **84**, 015601 (2011).

[71] O. Lailey, D. Sarenac, D. G. Cory, M. G. Huber, and D. A. Pushin, Unified quantum walk model for internal crystal effects in dynamical diffraction, Phys. Rev. A **114**, 032210 (2026).

[72] O. Lailey, Unified QI model code [Computer software], Zenodo, 2026, https://doi.org/10.5281/zenodo.23345317.